Progress in PHOTOVOLTAICS

PROGRESS IN PHOTOVOLTAICS: RESEARCH AND APPLICATIONS
Prog. Photovolt: Res. Appl. 2016; **24**:836–845
Published online 21 February 2016 in Wiley Online Library (wileyonlinelibrary.com). DOI: 10.1002/pip.2756

RESEARCH ARTICLE

The role of nanoparticle inks in determining the performance of solution processed $Cu_2ZnSn(S,Se)_4$ thin film solar cells

Yongtao Qu, Guillaume Zoppi and Neil S. Beattie*

Department of Physics and Electrical Engineering, Ellison Building, Northumbria University, Newcastle upon Tyne, NE1 8ST, UK

ABSTRACT

Cu_2ZnSnS_4 (CZTS) nanoparticle inks synthesized by the injection of metal precursors into a hot surfactant offer an attractive route to the fabrication of Earth-abundant $Cu_2ZnSn(S,Se)_4$ (CZTSSe) thin film photovoltaic absorber layers. In this work it is shown that the chemical reaction conditions used to produce CZTS nanoparticle inks have a fundamental influence on the performance of thin film solar cells made by converting the nanoparticles to large CZTSSe grains in a selenium rich atmosphere and subsequent cell completion. The reaction time, temperature and cooling rate of the nanoparticle fabrication process are found to affect doping level, secondary phases and crystal structure respectively. Specifically, prolonging the reaction offers a new route to increase the concentration of acceptor levels in CZTSSe photovoltaic absorbers and results in higher device efficiency through an increase in the open circuit voltage and a reduction in parasitic resistance. Quenching the reaction by rapid cooling introduces a wurtzite crystal structure in the nanoparticles which significantly degrades the device performance, while elevating the reaction temperature of the nanoparticle synthesis introduces a secondary phase Cu_2SnS_3 in the nanoparticles and results in the highest cell efficiency of 6.26%. This is correlated with increased doping in the CZTSSe absorber and the results demonstrate a route to controlling this parameter. © 2016 The Authors. *Progress in Photovoltaics: Research and Applications* published by John Wiley & Sons, Ltd.

KEYWORDS

CZTS; CZTSSe; nanoparticle ink; doping; photovoltaic

***Correspondence**

Neil S. Beattie, Department of Physics and Electrical Engineering, Ellison Building, Northumbria University, Newcastle upon Tyne NE1 8ST, UK.

E-mail: neil.beattie@northumbria.ac.uk

Received 17 April 2015; Revised 30 November 2015; Accepted 7 January 2016

1. INTRODUCTION

$Cu_2ZnSn(S,Se)_4$ (CZTSSe) is a promising photovoltaic material and experiencing rapid improvements in recent years because of its Earth-abundant constituents and outstanding optoelectronic properties [1–6]. Among the variety of techniques employed for the preparation of the absorber films, solution-based deposition and processing have the potential to provide low-cost scalable routes to produce photovoltaic devices with high efficiency. Such results include the current record efficiency for CZTSSe solar cells at 12.6% using a hydrazine-solution based method [7]. On the other hand, nanoparticle inks offer a non-toxic alternative. Deposited from the Cu_2ZnSnS_4 (CZTS) nanoparticle inks, CZTS precursor thin films annealed in the presence of Se can provide devices with efficiency as high as 9.0% [8].

Both CZTS and CZTSSe are known to be highly disordered as a consequence of high doping levels from native defects resulting in a band structure that can be described by a fluctuating potential model [9]. The doping levels are of fundamental importance as they determine the optoelectronic behavior of devices. We have recently developed an experimental procedure to tune the properties of CZTS nanoparticles *via* the chemical reaction conditions [10]. Wurtzite CZTS was formed at lower temperature whereas Cu_2SnS_3 (CTS) was present in the nanoparticles at higher temperature. The reaction time was also found to have a strong effect on the nanocrystals which became increasingly copper poor and zinc rich as the reaction

evolved. Additionally, the existence of wurtzite structure depends critically on the reaction cooling rate.

CZTS nanoparticle inks are the basis of the photovoltaic absorber layer; their impact on device performance has not yet been reported or investigated. In most cases it is assumed that the majority of CZTS nanoparticles have been converted into large grains and lose their direct influence on the device performance. However, below the top micron-scale grains, the metal-chalcogenide nanoparticles are still found present in the grain sub-layer creating a bi-layer absorber [11]. To the best of our knowledge there has been no detailed report linking the properties of the nanoparticle inks with the completed solar cell performance. In this work, we demonstrate that we can fabricate large grain CZTSSe thin films and control the concentration of dopants. This is shown to have a significant effect on the solar energy conversion efficiency of photovoltaic devices made from the films. Furthermore, the device performance is also found to be sensitive to the atomic arrangement of the CZTSSe crystal structure which is strongly influenced by the rate of reaction cooling.

2. EXPERIMENTAL PROCEDURE

2.1. Nanoparticle synthesis and ink preparation

CZTS nanoparticles were fabricated using a hot-injection method described previously [10]. Four types of nanoparticle inks were prepared by varying key reaction parameters: temperature, time or cooling mode. The control sample (sample A) was obtained by setting the reaction temperature to 225 °C for 30 min followed by slow cooling (~5 °C/min) under ambient laboratory conditions. The remaining three nanoparticle inks were fabricated by systematically changing one of the key reaction parameters as indicated in Table I. For quenched sample B, the reaction was quenched by rapidly cooling the reaction vessel in ice-water.

The as-synthesized CZTS nanoparticles were dispersed in toluene with a concentration of ~10 mg/ml. However, the ink needed to be concentrated further to yield efficient deposition. The CZTS precipitation was therefore dispersed into hexanethiol (95%, Sigma Aldrich) with the aid of sonication and then filtered through a 1 micron syringe filter (Whatman) to remove large agglomerates. The filtrate was then sonicated for 10 min to yield the final concentration of ~100 mg/ml.

Table I. Fabrication parameters for four types of nanoparticles.

Device	Temperature (°C)	Time (min)	Cooling rate (°C/min)
Control (A)	225	30	5
Quenched (B)	225	30	20
Hot (C)	255	30	5
Prolonged (D)	225	60	5

2.2. Thin film deposition

CZTS thin films were prepared by spin-coating ~30 µl of the ink onto a square Mo-coated glass or bare glass substrate (2.5 cm × 2.5 cm) at a rate of 1200 rpm for 5 s. The samples were then dried on a hot plate in air at 150 °C for 30 s and then at 300 °C for 30 s (hereafter "soft-baking") to remove the residual solvent. The thickness of the deposited thin films could be accurately controlled and reproduced by repeated spin coating and soft-baking procedures. A thickness of 1 µm was set for efficient light absorption in all thin films.

2.3. Photovoltaic device fabrication

In order to produce an efficient absorbing layer, the CZTS nanocrystal thin films need to undergo a recrystallization process where small nanoparticles are converted into large grains. This is achieved via a selenization process where the formation of the sulfoselenide compound CZTSSe through the Se–S anion exchange induces large-scale grain growth by dissolution of the parent CZTS and cation reordering in the selenium-based lattice. The as-deposited CZTS/Mo/glass films were placed inside of a graphite cylinder with 300-mg selenium pellets placed directly beneath the substrate. The furnace was evacuated and heated to 500 °C (~20 °C/min) where the temperature was held for 20 min in an argon atmosphere (~10 mbar).

The resulting CZTSSe thin films were converted into solar cell devices with the configuration: Mo/CZTSSe/CdS/i-ZnO/ITO/Ni-Al. The CdS buffer layer was deposited using a chemical bath. Deionized water was first poured into a double-walled beaker. After the temperature inside the beaker stabilized at 70 °C, $CdSO_4$ (2 mM) and ammonium (1.5 M) were added successively with a magnetic stir bar continuously stirred to form the solution. The CZTSSe films were then soaked in the solution for 2 min before thiourea (12 mM) was mixed into the solution. After the reaction, the samples were removed from the bath, rinsed with deionized water and dried under a nitrogen stream and then annealed at 200 °C for 10 min in air. The transparent oxide layers were deposited by sputtering ~60 nm-thick insulating ZnO (i-ZnO) and ~200 nm-thick indium tin oxide (ITO). Finally, the front contact grid was deposited by electron beam evaporation of Ni (~50 nm) and Al (~1 µm) through a shadow mask. Each substrate was defined by mechanical scribing into nine 0.16 cm^2 devices.

2.4. Experimental methods

The morphology of CZTS precursor thin films was investigated using tapping mode atomic force microscopy (AFM) using a Veeco Nanoscope multimode system. The structure of the CZTS nanocrystals was examined

DOI: 10.1002/pip

using X-ray diffraction (XRD) carried out with a Siemens D-5000 diffractometer using a Cu K_α radiation source ($\lambda = 0.15406$ nm for $K_{\alpha 1}$). The film morphology and composition were determined using a FEI Quanta 200 scanning electron microscope (SEM) equipped with Oxford Instruments energy dispersive X-ray spectroscopy (EDS). K_α X-ray emission lines for Cu, Zn, S and L_α for Sn were used for quantification. Raman spectroscopy was performed with a Renishaw inVia microscope using a 514-nm argon ion laser. The valence states of the constituent elements in the CZTS thin film were assessed using a Thermo Scientific K-Alpha X-ray Photoelectron Spectrometer (XPS) System with a monochromatic Al K_α X-ray source (1486.6 eV). A short sputter cleaning was applied before the scanning process to remove possible contamination on the top surface. Elemental depth profiling was performed by secondary ion mass spectroscopy (SIMS) using a Hiden Analytical gas ion gun and quadrupole detector. A primary Ar beam with an impact energy of 4 keV and beam current of 200 nA was used to sputter over a 500 µm × 500 µm rastered area. A gating area of 10% was used to remove side wall effects. Current density–voltage (*J–V*) measurements were performed in a four-point probe configuration using a Keithley 2400 series source meter. Samples were illuminated with an Abet Technologies Sun 2000 solar simulator with an AM1.5 spectrum set (100 mW/cm^2). The external quantum efficiency (EQE) measurements were operated using a double grating monochromator (Bentham Instruments, M300) with illumination normalized against calibrated silicon and germanium detector. Capacitance–voltage (*C–V*) measurements of the finished device were made in the dark using an Agilent E4980A Precision LCR Meter operating at 100 kHz frequency and 100 mV step with bias voltage from 0 to −1 V.

3. RESULTS AND DISCUSSION

3.1. CZTS precursor thin films prepared from nanoparticle inks

The as-deposited precursor control thin film appears smooth and is formed of densely packed, uniform spherical CZTS nanoparticles with diameter around 20 nm as shown in Figure 1 (a). Figure 1 (b) shows a representative cross-sectional SEM image of the 10-layer coating CZTS nanocrystal film on Mo/glass substrate. It can be seen that the film is uniform with a thickness of ~1 µm.

XPS was used to confirm that the chemical synthesis method resulted in the formation of Cu (I) valence states in the CZTS precursor thin film synthesized using control conditions. As shown in Figure 2 (a), the copper spectrum shows two narrow peaks at 931.9 and 951.8 eV, with a peak splitting of 19.9 eV. No satellite features at 943 eV of Cu (II) indicates the presence of Cu (I). For completeness, the zinc 2p peaks at 1022.1 and 1045.2 eV show a separation of 23.1 eV, consistent with the standard splitting

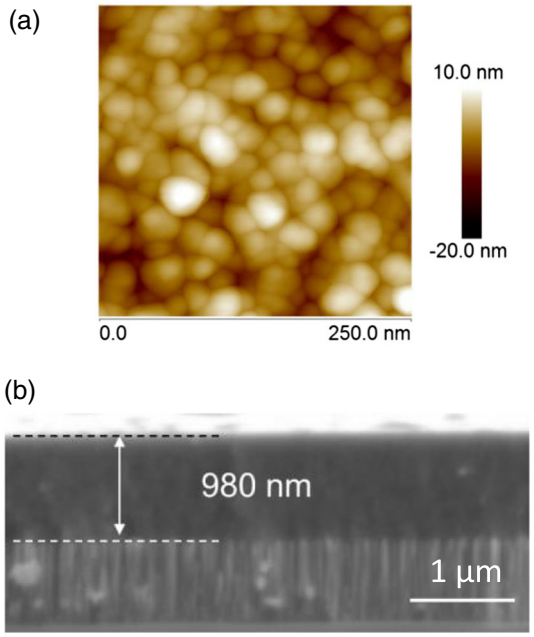

Figure 1. (a) AFM top view of the as-coated CZTS nanocrystal thin film, (b) cross-sectional SEM image of the as-coated CZTS nanocrystal film on Mo-coated glass substrate.

of 23 eV for Zn (II). The tin 3d peaks at 486.9 and 495.3 eV with a splitting of 8.4 eV indicate Sn (IV). The binding energies of S 2p 1/2 and S 2p 3/2 are 162.4 eV and 161.3 eV, respectively, revealing the valance state of S (−II).

The SIMS depth profiles of a CZTS precursor control thin film are shown in Figure 3. Except at the very surface of the thin film where the oxygen increases the ion yield of positive ions, the constituent elements of CZTS exhibit uniform distribution throughout the film thickness. The depth profile S/metals ratio is also shown as the dark solid line at the bottom of the graph which further demonstrates the uniformity of S and metals. The significant increase of Mo signal around 2100 s indicates the start of the CZTS/Mo interface. Combining the curves of Mo and S/metal ratio, the spectra can be divided into three compositional zones marked by the vertical lines. A MoS_2 layer is formed during the soft-baking process between the CZTS layer and Mo substrate. The C-rich solvent molecules are loosely bounded to the CZTS nanoparticles, and the soft-baking process allows to partially evaporate those molecules. However a diffusion process is required within the precursor film for this to happen, and it is conceivable that some of the C will diffuse towards the surface and evaporate while C diffusing towards the back of the film will start accumulating at the CZTS/Mo interface and result in the increase of C signal towards the interface with the substrate.

The crystal structure of the thin films fabricated using the four different nanoparticle inks was studied by XRD and Raman spectroscopy (Figure 4). As shown in Figure 4 (a), the major XRD diffraction peaks of the control

2016; **24**:836–845
DOI: 10.1002/pip

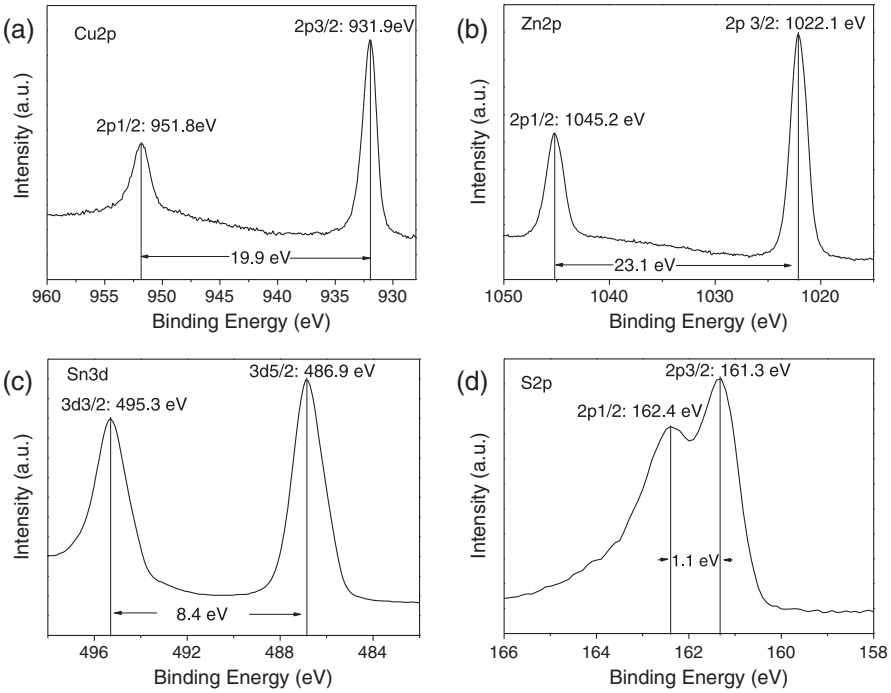

Figure 2. XPS spectra of Cu 2p, Zn 2p, Sn 3d and S 2p spectra of the CZTS precursor thin film.

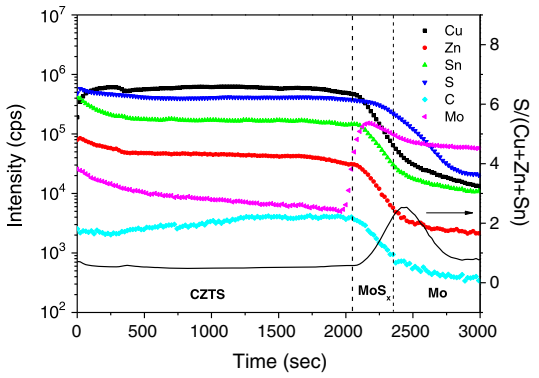

Figure 3. SIMS depth profiles of the CZTS precursor thin film deposited on Mo-coated glass. The dashed vertical lines divide the profile into three composition zones.

appear around 28°, 47° and 56°, which can be attributed to the (112), (220) and (312) planes of kesterite CZTS (PDF 026-0575), respectively. The quenched sample exhibits three weak diffraction peaks marked by asterisks shown in Figure 4 (a) in addition to the primary peaks. These belong to wurtzite CZTS co-existing in the nanoparticle ink because metastable wurtzite CZTS has insufficient time to complete the transformation to the more stable kesterite phase when the reaction temperature cools rapidly [10]. XRD patterns of the hot and prolonged samples have a similar pattern to kesterite CZTS with no obvious secondary phases observed.

Raman spectroscopy was used to further confirm the structure of the samples and rule out other binary or ternary compounds that have a similar XRD pattern to CZTS (Figure 4 (b)). For the control, the main peak located at 329 cm^{-1} is likely to be the A_1 mode of kesterite CZTS shifted downwards from 338 cm^{-1} because of the cation sublattice disorder for non-stoichiometric CZTS material. Because of the mixed atomic arrangement of kesterite and wurtzite phase, the main peak of the quenched sample broadens and shifts to 335 cm^{-1}. For the hot sample, a strong peak at 329 cm^{-1} corresponds to the A_1 mode of CZTS, although there is also a nearby shoulder peak at 301 cm^{-1}. This peak matches with either cubic CTS at 303 cm^{-1} or tetragonal CTS at 297 cm^{-1} [12]. For the prolonged sample, however, only one characteristic peak located at 329 cm^{-1} is observed, and has a similar spectrum to the control.

3.2. Preparation of CZTSSe photovoltaic absorber thin films

The selenization process was applied to the CZTS precursor thin films to convert the nanoparticles into micron-sized grains and minimize grain boundaries.

XRD was used to confirm the crystal structure of the selenized films. As shown in Figure 5 (a), the selenization process induces a sharpening of the diffraction peaks. All the peaks can be assigned to CZTSe (PDF 052-0868) slightly shifted to higher angles because of residual sulfur present in the lattice (Table II). As shown in Table II, the

DOI: 10.1002/pip

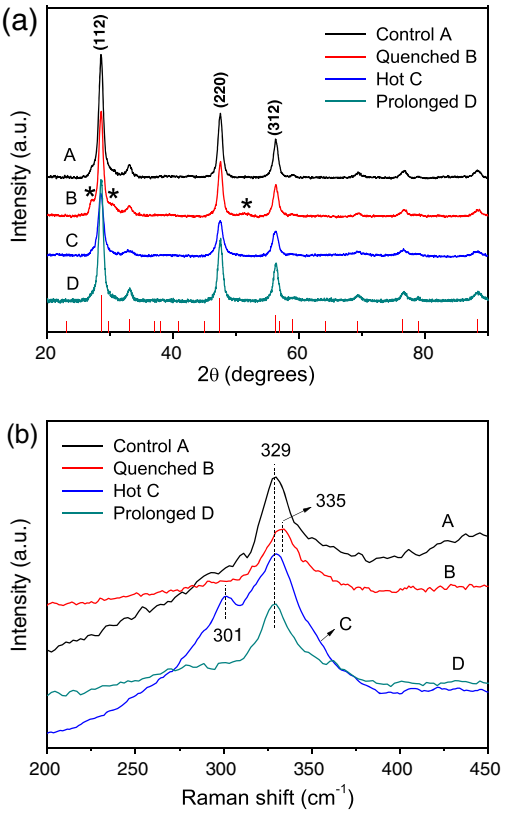

Figure 4. (a) XRD pattern of as-coated CZTS thin films compared to the reference pattern for kesterite CZTS (PDF 026-0575). (b) Raman spectra and of CZTS nanoparticles prepared at different reaction conditions. Diffraction patterns and Raman spectra are off-set for better visibility.

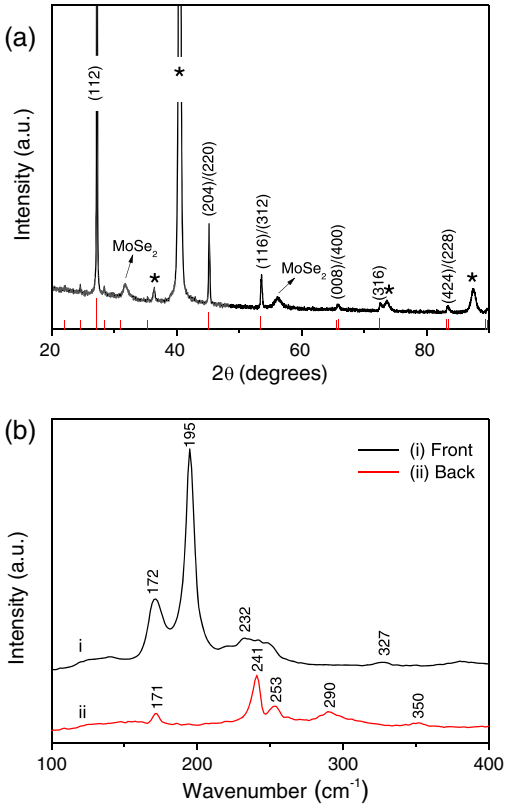

Figure 5. Crystal structure of CZTSSe film made from a control sample. (a) XRD pattern of the thin film compared to the reference pattern for pure CZTSe (PDF 052-0868). Peaks indexed to Mo are marked by * and $MoSe_2$ are also included. (b) Raman spectrum of the thin film front surface and the remaining substrate after mechanically removing the absorber. Spectra are off-set vertically for clarity.

composition of the selenized film is zinc rich and copper poor and about 90% anion exchange between sulfur and selenium occurs during the selenization process. A zinc loss was observed in the selenization process as the Cu/(Zn + Sn) ratio increased from 0.79 to 0.89 and the Zn/Sn ratio decreased from 1.15 to 1.

Raman spectroscopy was also performed on the selenized films and as shown in Figure 5 (b), the two sharp peaks at 172 and 195 cm^{-1}, and weak peaks at 232 cm^{-1} correspond to the literature values of CZTSe [13]. However, the shoulder peaks at the high frequency side of the 232 cm^{-1} are difficult to determine with accuracy. In addition, the wide peak at 327 cm^{-1} can be attributed to the A_1 mode of residual CZTS [14]. The ~10 cm^{-1} shift from the reported peak position of CZTS (~338 cm^{-1}) is likely because of the disorder or stress induced by the exchange between sulfur and selenium. In order to analyze the region close to the absorber/Mo interface, the measurement was repeated on the substrate after mechanically removing part of the absorber. As shown in Figure 5 (b), the spectrum from the substrate shows clear peaks at 241 and 253 cm^{-1} which can be identified as the main mode of $MoSe_2$ and ZnSe, respectively [15]. In addition, weaker peaks at 171, 290 and 350 cm^{-1} can all be indexed to $MoSe_2$.

As shown in Figure 6 (a), the cross-sectional image of the selenized thin film reveals a four-layer structure. The bottom layer is typical of Mo with a columnar grain structure. Under the selenium-rich annealing conditions, an approximately 0.5 μm thick layer of $Mo(S,Se)_2$ forms on top of the Mo layer by replacing part of the sulfur in MoS_2. Above the substrate, the CZTSSe layer is composed of a residual fine grain sublayer (~0.5 μm thick) and a large grain upper layer (~1 μm). Compared to the CZTS precursor thin film, the thickness of the CZTSSe thin film is increased because of the Se–S anion replacement and volume expansion of the CZTSSe unit cell during the selenization process.

The elemental distribution in the selenized film was studied using SIMS and shown in Figure 6 (b). Combined with the cross-sectional SEM image, the SIMS spectra can be divided into the four sections mentioned previously with different compositions. The large-grain layer is composed of high purity CZTSSe with low carbon content. The residual fine grain layer is rich in carbon, especially close to the substrate interface confirming our previous hypothesis of C being driven towards the back of absorber

 Progress in Photovoltaics: Research and Applications published by John Wiley & Sons, Ltd. 2016; **24**:836–845
DOI: 10.1002/pip

Table II. The composition of precursor and selenized thin films.

	Cu (at %)	Zn (at %)	Sn (at %)	S (at %)	Se (at %)	Cu/(Zn + Sn)	Zn/Sn	Se/(S + Se)
Pre-selenizaion	23.95	16.21	14.14	45.70	0	0.79	1.15	0
Post-selenization	22.35	12.62	12.65	5.75	46.63	0.89	1	0.89

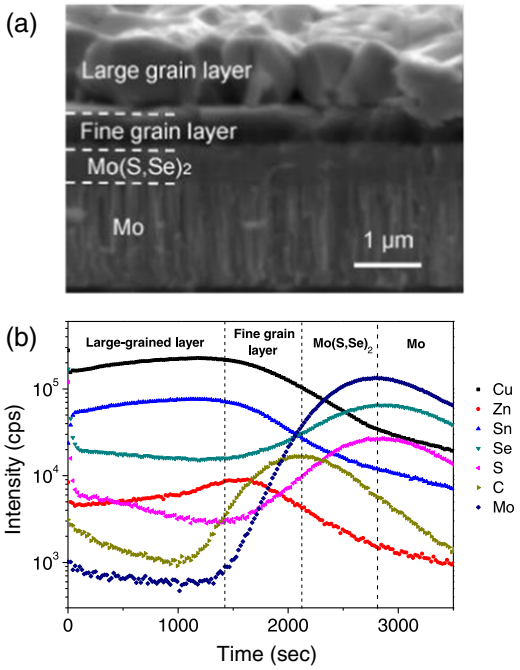

Figure 6. (a) Cross-sectional SEM image of the selenized control film (sample A). (b) SIMS depth profiles of the CZTSSe control film. The dashed vertical lines divide the profile into four composition zones.

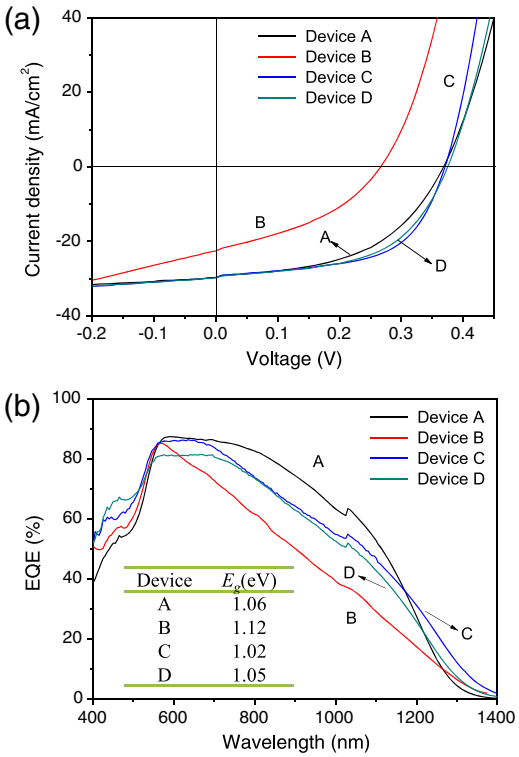

Figure 7. (a) *J–V* curves, (b) EQEs of devices A–D. The step in EQE spectra at 1030 nm is an artefact arising from a change in detector. The inset in (b) shows band gap energies E_g determined from the EQE spectra.

layer upon thermal annealing. The Raman analysis of the substrate after absorber removal also supports the presence of binary ZnSe in the fine grain layer [11]. A $Mo(S,Se)_2$ layer is formed above the Mo substrate because high levels of S and Se signals are found between the CZTSSe film and Mo substrate. Even in selenium-rich conditions, some residual sulfur is still present in the lattice. This agrees with the Raman spectra shown in Figure 5 (b) where a slight Raman shift is observed compared with literature position of the pure $MoSe_2$ [15].

3.3. Photovoltaic device performance

The CZTSSe thin films were converted into solar cell devices following the deposition of CdS, i-ZnO, ITO and Ni/Al contact layers. A series of four substrates was prepared (nine 0.16 cm^2 devices per substrate) using the four types of nanoparticle inks: control (sample A), quenched (sample B), hot (sample C) and prolonged (sample D). Devices differ only in the precursor ink used, and all other conditions were kept identical during the fabrication. Note that the devices do not include an anti-reflective coating.

J–V curves of the best device built on each substrate are shown in Figure 7 (a) with the device parameters extracted from the *J–V* curves summarized in Table III. Additionally, the distributions of solar energy conversion efficiency (η), open circuit voltage (V_{oc}), short circuit current density (J_{sc}) and fill factor (FF) of the nine devices on each substrate are shown in Figure 8 demonstrating the high uniformity of device performance across the substrates.

Baseline photovoltaic parameters for the control device can be derived from Figure 7(a): $\eta = 5.41\%$, $V_{oc} = 0.36$ V, $J_{sc} = 29.6$ mA/cm^2 and $FF = 50.7\%$. The most striking contrast to this set is found for the quenched reaction conditions as the presence of wurtzite phase CZTS has a profound effect on the efficiency of device B where $\eta = 2.30\%$, indicating that the reaction cooling mode which affects the atomic arrangement has a direct negative influence upon the device performance. The wurtzite phase in

DOI: 10.1002/pip

Table III. Device parameters for the solar cells with *J-V* curves shown in Figure 7.

Device	η (%)	V_{oc} (V)	J_{sc} (mA/cm^2)	*FF* (%)	R_S (Ω.cm^2)	R_{SH} (Ω·cm^2)	E_g-qV_{oc} (eV)
Control (A)	5.41	0.36	29.6	50.7	3.09	77	0.70
Quenched (B)	2.30	0.26	22.5	39.2	4.37	31	0.86
Hot (C)	6.26	0.37	29.7	57.0	1.86	116	0.65
Prolonged (D)	5.98	0.37	29.7	54.3	2.42	139	0.68

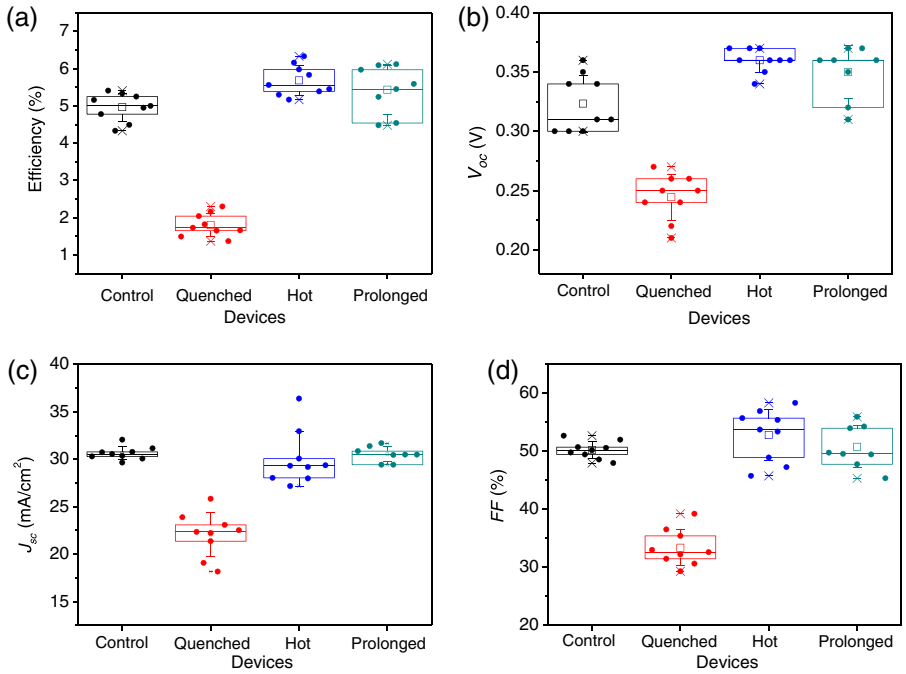

Figure 8. The distribution of (a) η, (b) V_{oc}, (c) J_{sc} and (d) *FF* of the nine devices on each substrate. □ is the average value. × is the minimum and maximum position. The three horizontal lines of each box stand for the 25%, 50% and 75% of the reading distribution. The whisker range is determined by the standard deviation of the nine readings.

the nanoparticles is thermodynamically unstable and tends to convert into stable kesterite phase during the selenization process [16]. The crystal structure difference between the wurtzite and kesterite structure may hinder the grain growth in the selenization process and results in small grains as observed in Figure 9. This is a new and important insight not least because this fabrication technique for synthesis of CZTS nanocrystals is widely reported in the literature. As shown in Table III, the reduced efficiency of this device arises not only from reductions in V_{oc} and J_{sc}, but also a large drop in *FF* caused by higher series resistance (R_S) and lower shunt resistance (R_{SH}). From the top view SEM images shown in Figure 9 (a), the selenized thin film made from sample A is composed of densely packed grains that can be up to 2 µm, with no obvious voids or cracks on the surface. However, as can be seen in Figure 9 (b), the grain size of the CZTSSe film made from the quenched sample is significantly smaller than that of the control. Considering the sheet resistance of the Mo and ITO is 0.2 Ω/□ and 35 Ω/□, respectively, the increased parasitic resistance of the quenched device is likely derived from increased density of grain boundaries which act as recombination centers. It is possible that wurtzite phase CZTS undergoes a phase transition to kesterite during the selenization stage [16]; however, this wurtzite CZTS may hinder the grain growth process and even present a residual component that significantly degrades device performance. Figure 7 (a) also shows the *J–V* characteristic for the devices with hot and prolonged reaction conditions (C and D respectively). These devices have higher solar energy conversion efficiencies relative to the control, and this is manifested through higher fill factors which in turn are determined by R_S and R_{SH}. The former is likely to be influenced by the unconverted nanocrystals and the Mo(S,Se_2) layer at the back of the device [8] while R_{SH} is influenced by the CZTSe grain size. Analysis of Figure 9 reveals that the prolonged reaction time results in a selenized thin film that has slightly larger grains (Figure 9 (d)) compared with the hot reaction condition (Figure 9 (c)). This reduces the number of grain boundaries and, in turn, the number of shunt pathways [17] and is evidenced by the higher R_{SH} value.

2016; **24**:836–845
DOI: 10.1002/pip

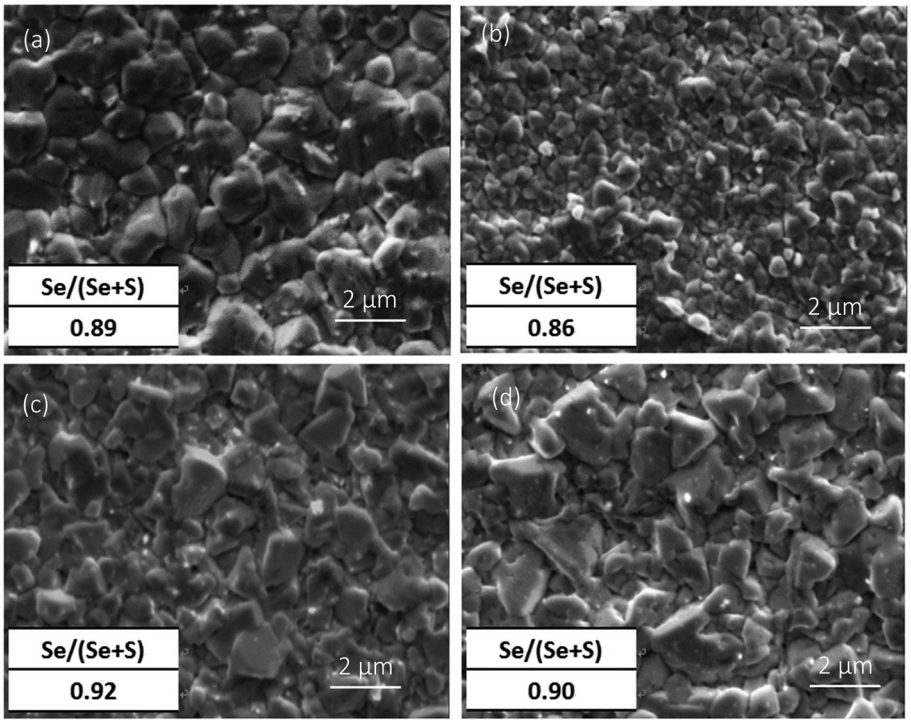

Figure 9. Top view SEM images of CZTSSe film made from (a) sample A, (b) sample B, (c) sample C and (d) sample D. The insets show the Se/(Se + S) ratios of the films.

The EQE spectra of the devices (Figure 7 (b)) show behavior that is consistent with the *J–V* characteristics. All devices show less ideal EQE toward longer wavelengths which is a result of recombination losses that can attributed to the fine grain and $MoSe_2$ layers [14], and future work will focus on reducing the influence of these on performance. In addition, the spectrum for the quenched device ($E_g = 1.12$ eV) is exhibiting a strong triangular shape indicative of severe current collection losses. This could arise from short electron diffusion length and high doping density (see analysis of capacitance measurements). The variations in energy band gap derived from the band tail of the EQE spectra are consistent with the fluctuations in Se/(Se + S) ratios as measured by EDS (Figure 9 insets). It is interesting to note that sample B yields less Se incorporation into the CZTS lattice compared to the other three processes which have similar Se/(Se + S) ratio at around 0.90.

The hot device (device C) exhibits the highest overall efficiency of $\eta = 6.26\%$, with $V_{oc} = 0.37$ V, $J_{sc} = 29.7$ mA/cm^2 and $FF = 57.0\%$. Raman spectroscopy (Figure 4 (b)) revealed that this film contained secondary phase CTS, and this champion efficiency correlates with the current world record efficiency for CZTSe thin films fabricated using selenization of CZTS nanoparticles which were also found to contain CTS [8]. The reason for this is not currently well-understood and merits further investigation.

C–V measurements were performed to estimate the doping density (N_A), the built in potential (V_{bi}) and depletion layer width (W) in the CZTSSe absorber layer of the completed devices. Figure 10 shows a plot of $1/C^2$ versus reverse bias voltage for the devices and from the slope and intercept of the linear fits, N_A and V_{bi} can be determined respectively. Additionally, the width of the depletion region in each region W can be deduced from the data. These values for all four samples are listed in Table IV where the values are comparable to vacuum [18] or hydrazine-based CZTS [7] fabrication methods confirming that there is no loss of junction quality using the nanocrystal fabrication route.

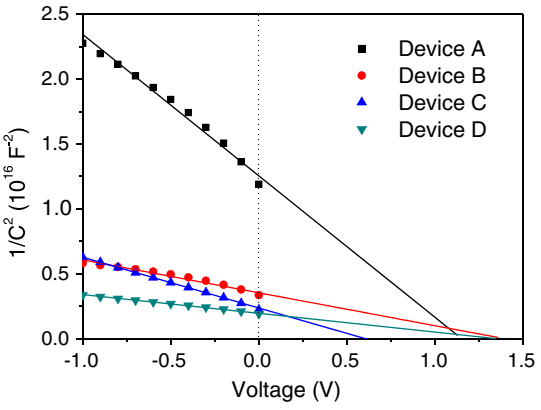

Figure 10. $1/C^2$ versus reverse bias voltage plots of devices A–D.

DOI: 10.1002/pip

Table IV. Parameters extracted from C–V measurements.

Device	N_A (cm^{-3})	W (nm)	V_{bi} (V)
Control (A)	4.4×10^{16}	117	1.14
Quenched (B)	2.8×10^{17}	62	1.36
Hot (C)	2.0×10^{17}	51	0.62
Prolonged (D)	5.3×10^{17}	47	1.35

CZTSSe is usually reported to be *p*-type arising from a large number of Cu vacancies V_{Cu}^{-}, although antisite defects such as Zn_{Cu} and Cu_{Zn} are also common [19]. Comparisons between all four devices in terms of doping are difficult because the crystal structure has been shown to be markedly different between the samples and therefore cannot easily be attributed to the density of V_{Cu}^{-} (despite all absorbers being Cu poor). However, we have demonstrated a high degree of similarity between the control and the prolonged samples and devices, and the most obvious discrepancy is indeed N_A which is an order of magnitude higher for the prolonged sample. It is this parameter that results in a higher solar energy conversion efficiency and to the best of our knowledge the first experimental demonstration that the doping density can be increased without changing the crystal structure of a CZTSSe absorber synthesized from nanoparticle inks. The increase in efficiency derives from small increase in average V_{oc} for the prolonged device and a reduction in fill factor.

Although the interpretation of the *C–V* data for the quenched and hot devices is more difficult, we suggest that the increased values of N_A for these devices relative to the control are a consequence of increased disorder in the crystal structure. The case of the hot device is particularly interesting because it results in the highest efficiency of all the devices. This is consistent with the earlier analysis of the doping concentration between the control and the prolonged device. The key difference here however, is that we have correlated the higher reaction temperature with the presence of secondary phase CTS. These findings are important in the context of work by Miskin *et al*. who recently demonstrated a CZTSSe nanoparticle ink solar cell with $\eta = 9\%$ (with an anti-reflection coating) [8] but do not account for an experimentally observed CTS phase which has previously been thought to be detrimental to solar cell performance because of a narrower energy band gap. Our results indicate that the apparent positive effects of CTS may be because of an effective increase in the absorber doping which in turn enhances V_{oc} in the device. The apparent increase in V_{oc} is seen more clearly by considering that the voltage deficit (E_g-qV_{oc}) (also shown in Table III) is minimized for the hot device. It has been shown that CTS may precipitate at the CZTS grain boundaries [20], where the minority carrier collection can also be enhanced [21]. Additionally, the CTS precipitation could provide some grain boundary passivation and thus explain the increase in device performance observed.

Solving Poisson's equation for the electric field in the *n*-type and *p*-type regions of a *pn* junction yields a dependence on the density of donors and acceptors respectively. Continuity of the field requires that the width of the depletion region varies inversely with doping concentration, i.e. that the depletion region extends into the side with the lowest doping. This is consistent with the control device having the largest value of W in Table IV and the highest EQE in the 700–1150 nm range testimony of the better charge collection in that device. The values of V_{bi} are similar apart from the hot sample, and this is likely attributable to the presence of CTS which reduces the energy band gap of the absorber.

4. CONCLUSIONS

High quality CZTSSe photovoltaic absorber layers were fabricated from CZTS nanoparticle inks by annealing stacked layers of nanoparticles in a selenium rich atmosphere. These were subsequently incorporated into thin film solar cells, and the device performance has been found to depend critically upon the chemical reaction conditions used to synthesize the nanoparticles. Crucially, rapid thermal quenching of the reaction results in wurtzite CZTS in the nanoparticles. This results in smaller grains and an increase in the number of grain boundaries in the CZTSSe thin film absorber layers which are strongly detrimental to the device performance. Prolonging the reaction offers a new route to increasing the concentration of acceptor levels in CZTSSe photovoltaic absorbers and results in higher device efficiency relative to a control device. The presence of CTS correlates with increased efficiency, and the apparent positive effects of this phase are also accompanied by an increase in the doping levels. To fully exploit doping control in these devices, we propose that it will be essential to minimize any negative effects of the fine grain sub-layer below the CZTSSe grains that are commonly found in this type of solar cell.

ACKNOWLEDGEMENTS

NB and GZ gratefully acknowledge funding from the Royal Society (Research Grant R120090). X-ray photoelectron spectra were obtained at the National EPSRC XPS User's Service (NEXUS) at Newcastle University, an EPSRC Mid-Range Facility. Access to Raman spectroscopy was enabled by the EPSRC Engineering Instrument Pool.

REFERENCES

1. Zhou H, Hsu WC, Duan HS, Bob B, Yang W, Song TB, Hsu CJ, Yang Y. CZTS nanocrystals: a promising approach for next generation thin film photovoltaics. *Energy & Environmental Science* 2013; **6**: 2822–2838. DOI:10.1039/c3ee41627e.

2. Repins I, Beall C, Vora N, DeHart C, Kuciauskas D, Dippo P, To B, Mann J, Hsu WC, Goodrich A, Noufi R. Co-evaporated $Cu_2ZnSnSe_4$ films and devices. *Solar Energy Materials and Solar Cells* 2012; **101**: 154–159. DOI:10.1016/j.solmat.2012.01.008.
3. Shin B, Gunawan O, Zhu Y, Bojarczuk NA, Chey SJ, Guha S. Thin film solar cell with 8.4% power conversion efficiency using an earth-abundant Cu_2ZnSnS_4 absorber. *Progress in Photovoltaics: Research and Applications* 2013; **21**: 72–76. DOI:10.1002/pip.1174.
4. Yang W, Duan HS, Bob B, Zhou H, Lei B, Chung CH, Li SH, Hou WW, Yang Y. Novel solution processing of high-efficiency earth-abundant $Cu_2ZnSn(S,Se)_4$ solar cells. *Advanced Materials* 2012; **24**: 6323–6329. DOI:10.1002/adma.201201785.
5. Winkler MT, Wang W, Gunawan O, Hovel HJ, Todorov TK, Mitzi DB. Optical designs that improve the efficiency of $Cu_2ZnSn(S,Se)_4$ solar cells. *Energy & Environmental Science* 2014; **7**: 1029–1036. DOI:10.1039/c3ee42541j.
6. Zoppi G, Forbes I, Miles RW, Dale PJ, Scragg JJ, Peter LM. $Cu_2ZnSnSe_4$ thin film solar cells produced by selenisation of magnetron sputtered precursors. *Progress in Photovoltaics: Research and Applications* 2009; **17**: 315–319. DOI:10.1002/pip.886.
7. Wang W, Winkler MT, Gunawan O, Gokmen T, Todorov TK, Zhu Y, Mitzi DB. Device characteristics of CZTSSe thin-film solar cells with 12.6% efficiency. *Advanced Energy Materials* 2014; **4**: 131465. DOI:10.1002/aenm.201301465.
8. Miskin CK, Yang WC, Hages CJ, Carter NJ, Joglekar CS, Stach EA, Agrawal R. 9.0% efficient $Cu_2ZnSn(S,Se)_4$ solar cells from selenized nanoparticle inks. *Progress in Photovoltaics: Research and Applications* 2015; **23**: 654–659. DOI:10.1002/pip.2472.
9. Mendis BG, Shannon MD, Goodman MCJ, Major JD, Claridge R, Halliday DP, Durose K. Direct observation of Cu, Zn cation disorder in Cu_2ZnSnS_4 solar cell absorber material using aberration corrected scanning transmission electron microscopy. *Progress in Photovoltaics: Research and Applications* 2014; **22**: 24–34. DOI:10.1002/pip.2279.
10. Qu Y, Zoppi G, Miles RW, Beattie NS. Influence of reaction conditions on the properties of solution-processed Cu_2ZnSnS_4 nanocrystals. *Materials Research Express* 2014; **1**: 045040. DOI:10.1088/2053-1591/1/4/045040.
11. Wu W, Cao Y, Caspar JV, Guo Q, Johnson LK, Malajovich I, Rosenfeld HD, Choudhury KR. Studies of the fine-grain sub-layer in the printed CZTSSe photovoltaic devices. *Journal of Materials Chemistry C* 2014; **2**: 3777–3781. DOI:10.1039/c4tc00391h.
12. Fernandes PA, Salomé PMP, da Cunha AF. Study of polycrystalline Cu_2ZnSnS_4 films by Raman scattering. *Journal of Alloys and Compounds* 2011; **509**: 7600–7606. DOI:10.1016/j.jallcom.2011.04.097.
13. Cao Y, Denny MS, Caspar JV, Farneth WE, Guo Q, Ionkin AS, Johnson LK, Lu M, Malajovich I, Radu D, Rosenfeld HD, Choudhury KR, Wu W. High-efficiency solution-processed $Cu_2ZnSn(S,Se)_4$ thin-film solar cells prepared from binary and ternary nanoparticles. *Journal of the American Chemical Society* 2012; **134**: 15644–15647. DOI:10.1021/ja3057985.
14. van Embden J, Chesman ASR, Della Gaspera E, Duffy NW, Watkins SE, Jasieniak JJ. $Cu_2ZnSnS_4xSe_{4(1-x)}$ solar cells from polar nanocrystal Inks. *Journal of the American Chemical Society* 2014; **136**: 5237–5240. DOI:10.1021/ja501218u.
15. Redinger A, Hönes K, Fontané X, Izquierdo-Roca V, Saucedo E, Valle N, Pérez-Rodríguez A, Siebentritt S. Detection of a ZnSe secondary phase in coevaporated $Cu_2ZnSnSe_4$ thin films. *Applied Physics Letters* 2011; **98**: 10107. DOI:10.1063/1.3558706.
16. Yang WC, Miskin CK, Hages CJ, Hanley EC, Handwerker C, Stach EA, Agrawal R. Kesterite $Cu_2ZnSn(S,Se)_4$ absorbers converted from metastable, wurtzite-derived Cu_2ZnSnS_4 nanoparticles. *Chemistry of Materials* 2014; **26**: 3530–3534. DOI:10.1021/cm501111z.
17. Williams BL, Smit S, Kniknie BJ, Bakker KJ, Keuning W, Kessels WMM, Schropp REI, Creatore M. Identifying parasitic current pathways in CIGS solar cells by modelling dark J–V response. *Progress in Photovoltaics: Research and Applications* 2015. DOI:10.1002/pip.2582.
18. Fernandes PA, Salomé PMP, Sartori AF, Malaquias J, da Cunha AF, Schubert BA, González JC, Ribeiro GM. Effects of sulphurization time on Cu_2ZnSnS_4 absorbers and thin films solar cells obtained from metallic precursors. *Solar Energy Materials and Solar Cells* 2013; **115**: 157–165. DOI:10.1016/j.solmat.2013.03.032.
19. Chen S, Gong XG, Walsh A, Wei SH. Defect physics of the kesterite thin-film solar cell absorber Cu_2ZnSnS_4. *Applied Physics Letters* 2010; **96**: 021902. DOI:10.1063/1.3275796.
20. Mendis BG, Goodman MCJ, Major JD, Taylor AA, Durose K, Halliday DP. The role of secondary phase precipitation on grain boundary electrical activity in Cu_2ZnSnS_4 (CZTS) photovoltaic absorber layer material. *Journal of Applied Physics* 2012; **112**: 124508. DOI:10.1063/1.4769738.
21. Li JB, Chawla V, Clemens BM. Investigating the role of grain boundaries in CZTS and CZTSSe thin film solar cells with scanning probe microscopy. *Advanced Materials* 2012; **24**: 720–723. DOI:10.1002/adma.201103470.

DOI: 10.1002/pip